# Studies of intermediate-mass fragment emission in the $^{3}He+^{nat}Ag$, $^{197}Au$ reactions between 0.48 and 3.6 GeV

S. J. Yennello,[1,2,*] K. Kwiatkowski,[1] E. C. Pollacco,[2] C. Volant,[2] Y. Cassagnou,[2] R. Dayras,[2] D. E. Fields,[1] S. Harar,[2,3] E. Hourani,[4] R. Legrain,[2] E. Norbeck,[5] R. Płaneta,[1,6] J. L. Wile,[1,†] N. R. Yoder,[1] and V. E. Viola[1]

[1]*Indiana University, Bloomington, Indiana 47405*

[2]*DAPNIA/Service de Physique Nucléaire, Centre d'Etudes Nucléaires de Saclay, F-91191, Gif-sur-Yvette, France*

[3]*Grand Accélérateur National d'Ions Lourds (GANIL), Boîte Postale No. 5027, boulevard Henri Becquerel, 14021 Caen Cédex, France*

[4]*Institut de Physique Nucléaire, Orsay, Boîte Postale F-91406, Orsay, France*

[5]*Iowa University, Iowa City, Iowa 52242*

[6]*Jagellonian University, Krakow, Poland*

(Received 1 February 1993)

Intermediate-mass fragments formed in reactions of $^{3}He$ ions with $^{nat}Ag$ and $^{197}Au$ targets have been studied at five energies between 0.48 and 3.6 GeV. Inclusive measurements show that as the bombarding energy increases, there is a strong enhancement in fragment cross sections and a trend toward isotropic angular distributions. Between 0.90 and 1.8 GeV, a change in the emission mechanism is suggested by (1) kinetic energy spectra with high-energy tails that become distinctly flatter, (2) a broadening of the spectral Coulomb peaks toward lower energies, and (3) charge distributions that become constant, exhibiting a power-law exponent $\tau \approx 2.0$. Exclusive studies of the $^{3}He+^{nat}Ag$ system at 0.90 and 3.6 GeV detected multifragment events with multiplicities up to four. The probability for high-multiplicity events increases about 40-fold between 0.90 and 3.6 GeV. At both energies, the kinetic energy spectra depend on multiplicity, especially when triggering on backward-emitted fragments. For multiplicity three events, a rapidity analysis of the data at 3.6 GeV is consistent with a single, relatively low source velocity, $v_S \approx 0.4$ cm/ns. The data are compared with predictions of a coplanarity-sphericity calculation, the sequential statistical decay code GEMINI, and a hybrid intranuclear cascade/percolation model.

PACS number(s): 25.55.−e

## I. INTRODUCTION

Accounting for the emission of intermediate-mass fragments (IMF's) from highly excited nuclei produced in intermediate-energy reactions poses a severe challenge for experimentalists and theorists alike. These ejectiles are usually defined as fragments with atomic numbers $3 \leq Z \lesssim 15$, i.e., heavier than light-charged particles (LCP=H and He), but lighter than fission fragments. IMF's were initially detected over 30 years ago in radiochemical studies of proton- and alpha-particle-induced reactions on heavy target nuclei [1–3]. These early measurements were especially important in demonstrating that the probability for IMF emission increases strongly up to bombarding energies of several GeV, thus associating these events with the disintegration of highly excited nuclei [4,5]. In addition, these early studies stimulated many discussions relating to the question of energy dissipation on a very fast time scale and the possible role of subnucleonic degrees of freedom and density compressions in such processes [1,4]. The concept of multifragmentation—or the disintegration of hot nuclei on a time scale comparable to the collision time—also emerged in response to these results.

Multifragment emission, i.e., final states involving two or more IMF's, is a subject of intense current interest. Evidence for such events has been indicated on the basis of emulsion studies [2,4–6] and has been demonstrated in several recent counter experiments with heavy ions [7–12]. An important question concerning these data is the distinction between a sequence of statistical binary decays and breakup of the system on a faster time scale (or multifragmentation) [13]. In the former case, the mechanism represents the simple compounding of a series of statistical emission probabilities. Such contributions must certainly be present in energetic reactions, especially with heavy-ion projectiles, due to the known angular momentum enhancement of the IMF emission probability [14–16]. Multifragmentation, on the other hand, may represent a unique phenomenon [17–23], although clear-cut experimental verification remains to be firmly established. Given the very short lifetimes expected for systems at high excitation energies, the difference between sequential and instantaneous decay may not be easily distinguishable. Understanding these complex processes demands both systematic experimental studies involving multidetector, large solid-angle arrays, and theoretical efforts which combine the collision and decay dynamics self-consistently.

*Present address: Department of Chemistry, Texas A&M University, College Station, TX 77843.

†Present address: Ball State University, Muncie, IN 47306.

 

Investigation of IMF emission in light-ion-induced reactions on heavy target nuclei affords several experimental features of utility in attempts to understand the multifragmentation process. Among these are (1) emission from a single source, (2) minimal kinematic distortions of the spectra, (3) forward-angle yields free from projectile-like IMF's, and (4) minimum angular momentum. In addition, such measurements provide an important base line for deducing compressional effects in heavy-ion-induced reactions. The present experiments have examined the $^{3}$He+$^{nat}$Ag and $^{197}$Au reactions between energies of 0.48 MeV and 3.6 GeV. These data complement lower-energy measurements of the $^{3}$He+$^{nat}$Ag reaction [16,24], thus providing a rather complete excitation function for inclusive variables. Related studies with $^{4}$He projectiles have also been carried out by Klotz-Engmann *et al.* [25] and Avdeichikov *et al.* [26]. Several inclusive measurements of IMF's with proton beams have preceded these studies [5,27–34].

In this paper we first describe inclusive excitation function studies of the $^{3}$He+$^{nat}$Ag and $^{197}$Au reactions. These results [35] indicated a change in the character of the IMF emission mechanism above 1 GeV, similar to that observed in Ref. [27]. A multifold coincidence experiment was then performed [11] in order to investigate multiple IMF emission at 0.90 and 3.6 GeV, just below and well above the indicated transition region [35]. These data are discussed in the context of several models for IMF emission.

## II. EXPERIMENTAL PROCEDURES

The experiments were performed using the SATURNE II accelerator at the Laboratoire National Saturne in Saclay, France. Beams of total energy 0.48, 0.90, 1.8, 2.7, and 3.6 GeV $^{3}$He ions bombarded high-purity targets of $^{nat}$Ag and $^{197}$Au. The sequence of beam energies was 0.48, 1.8, 3.6, 0.90, 2.7 GeV for the inclusive measurements. This order was chosen to minimize any systematic changes in the target or detector system as a function of time. The coincidence experiments were also performed at the SATURNE II accelerator. Data were taken for two beam energies, 0.90 and 3.6 GeV $^{3}$He. This provided data at energies above and below the energy at which a reaction mechanism change was seen in the inclusive measurements [35].

For the inclusive experiment, high-purity, self-supporting targets of 1.15 and 1.36 mg/cm$^2$ $^{nat}$Ag and 2.09 mg/cm$^2$ $^{197}$Au were mounted on a target ladder, along with a scintillator for focusing the beam, a blank frame to study events arising from any beam halo, and a 415-$\mu$g/cm$^2$ C target for light-element background evaluation. The spectra did not show any significant contribution from light-element contamination. The coincidence experiment used two high-purity $^{nat}$Ag targets of thicknesses 0.92 and 0.88 mg/cm$^2$, sequentially exposed to the beam. Blank targets, run periodically, showed the absence of beam halo contributions to the data. Typical beam intensities on target were about $10^{10}$ particles/burst for the inclusive studies and $10^{9}$ particles/burst for the exclusive measurements, with a burst length of 300–400 ms and a repetition rate of about 1.5 s. The beam intensity was monitored with a secondary emission monitor. The absolute normalization was determined by irradiation of a carbon target and off-line counting of the $^{11}$C activity; cross sections for the $^{12}$C($^{3}$He$2p2n$)$^{11}$C reaction were taken to be 62.5 mb at 0.90 GeV and 55 mb at 3.6 GeV [36].

During the coincidence experiment, the quality of the beam was monitored by a pair of concentric active 6-mm-thick plastic scintillator collimators with a 19-mm-thick hole placed at the front entrance to the scattering chamber. By mounting these two devices perpendicular to one another, a two-dimensional reading of any beam halo and its correlation with the time structure of the beam were obtained.

In the inclusive experiment, complex fragments were measured with an array of five particle-identification telescopes placed at fixed angles between 60° and 160°. Telescopes at 60°, 90°, and 140° were composed of an axial-field gas-ionization chamber (GIC), followed by a 300-$\mu$m surface barrier silicon detector [Si(SB)], and a 5-mm lithium-drifted silicon detector [Si(Li)]. The telescope at 120° was a large-area GIC, followed by two 300-$\mu$m passivated silicon detectors of area 25-cm$^2$ [37]. The telescope at 160° was a longitudinal-field GIC and a 500-$\mu$m Si(SB) detector. Angles from 15° to 45° were covered by a sixth telescope positioned on a movable arm consisting of an axial-field GIC, followed by a 75-$\mu$m Si(SB), 300-$\mu$m Si(SB), and a 5-mm Si(Li) detector. The respective solid angles were 2.08 msr (60°), 5.45 msr (90°), 5.39 msr (140°), 8.61 msr (120°), 5.34 msr (160°), and 3.9 msr (forward angles). Each GIC had a 1.5-$\mu$m Mylar window, an active length of 6 cm, and operated at approximately 20 torr of $CF_4$. Rare-earth magnets were placed on the front of each ionization chamber for electron suppression.

In the coincidence experiment, complex fragments were measured with an array of 36 particle-identification telescopes that covered a total solid angle of approximately 1 sr or 8% of $4\pi$. The basic detector elements consisted of an axial-field GIC $\Delta E$ detector (1.5-$\mu$m Mylar window and 2.5-$\mu$m aluminized Mylar anode) with an active length of 6 cm and operated at about 20 torr of $CF_4$, and a passivated silicon $E$ detector 500 $\mu$m thick and 25 cm$^2$ in area. Thirty-two of these detector telescopes made up a global array, arranged to provide approximately random coverage of the available solid angle. Telescopes were arranged in quad units with a common gas volume. The quad units were set on three rings, each at a constant angle with respect to the beam axis (35°, 64°, and 117°). The 35° units each had a solid angle of 73 msr, while the units on the other two rings had solid angles of 140 msr. The units on a particular ring were separated by 120° in azimuthal angle phi, and each ring was offset by 40° in phi from the other rings. Four additional telescopes, placed at 25°, 63°, 107°, and 149°, consisted of a GIC followed by a 200-$\mu$m passivated silicon detector and either by a 300- or 500-$\mu$m passivated silicon detector. These were also followed by a scintillator capable of stopping up to 70 MeV/nucleon LCP's. These four detectors composed a planar array. These detector configurations provided definition of the complex frag-

ment energy spectra from about $E/A \approx 0.6$ MeV up to the maximum energy produced in these reactions.

During the inclusive experiment, alpha-particle rejection was set up in hardware, since about 90% of the events were H and He ions. In this way all IMF's were accepted and all but the very-low-energy protons and alpha particles were rejected. Since SATURNE II is a synchrotron and the energy must be ramped for each beam spill, accurate dead-time corrections and integrated current readings mandated that the electronics be gated by the beam-burst valid signal.

The coincidence experiment electronics were set up to allow either singles or coincidence data to be acquired, and to allow events to be triggered by either a valid signal in the silicon detector or a coincidence between the silicon detector and the ion chamber of an individual telescope.

More complete experimental details are contained in Ref. [38].

## III. INCLUSIVE RESULTS

In Fig. 1 the angular distributions for complex fragments obtained in this work are compared with lower-energy $^3$He+$^{nat}$Ag data, where IMF emission has been shown to occur by both statistical decay from an equilibriumlike source and nonequilibrium emission on a fast time scale [16,24]. Most evident in this plot is the strong increase in cross section as a function of bombarding energy, approximately three orders of magnitude for carbon fragments at 90° between 90 MeV and 3.6 GeV. This increase becomes more pronounced as the atomic number of the IMF increases. The evolution of the angular distributions as a function of bombarding energy suggests the changing character of the mechanism for IMF production. At an incident energy of 90 MeV, the angular distributions exhibit a slight backward peaking relative to 90°; at 200 MeV, the angular distributions decrease rapidly from 0° to 90°, but become nearly isotropic thereafter.

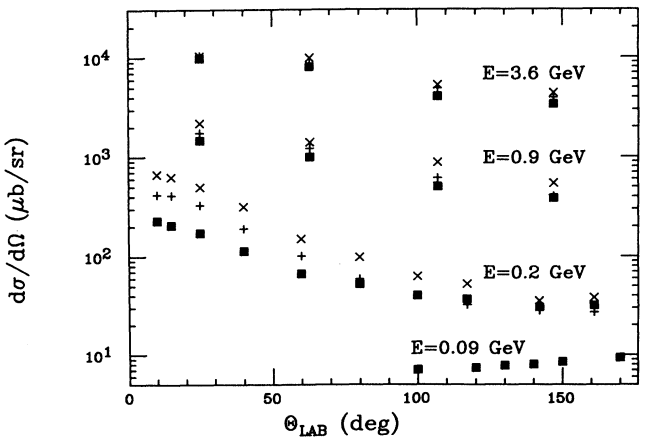


FIG. 1. Angular distributions of complex fragments emitted from the $^3$He+$^{nat}$Ag system at bombarding energies indicated. The 90-MeV data are from Ref. [24], and the 200-MeV data are from Ref. [16]. Symbols are as follows: Be (×), B (+), and C (■).

Beyond 0.48 GeV the differential cross sections decrease monotonically with increasing angle, with the slope becoming increasingly flat at the higher energies. This latter effect is largely due to the increase in probability for emission of fragments at backward angles. Table I lists the differential and angle-integrated cross sections for 0.90- and 3.6-GeV bombardments of $^{nat}$Ag, respectively.

Figures 2–4 illustrate the evolution in the energy spectra as a function of $^3$He bombarding energy and angle of emission for several representative IMF's. Figure 2 shows the complete data set for carbon ejectiles; Figs. 3 and 4 show forward and backward spectra for $Z=4$, 5, and 6 IMF's from the $^{nat}$Ag and $^{197}$Au targets, respectively. For each bombarding energy, the spectral shapes are characterized by increasingly steep high-energy slopes as the angle of emission increases. This behavior is most pronounced at 0.48 and 0.90 GeV, where the spectra strongly resemble those obtained at lower energies [16]. However, for bombarding energies above 0.90 GeV, the spectral slopes show a less pronounced decrease with angle.

When the fragment kinetic energy distributions for a fixed angle are compared as a function of projectile energy, it is observed that the spectral slopes for the forward-angle data appear similar, with somewhat flatter spectra at the higher energies. Most striking, however, is the comparison at backward angles. Here a transition in the character of the spectra appears to occur between 0.90 and 1.8 GeV for the $^{nat}$Ag target and near 1.8 GeV for $^{197}$Au. Further, the spectra for a given angle are virtually identical in shape for the three highest energies, although the yields continue to increase. Thus analysis of the exponential slopes of the high-energy portion of these spectra suggests that at incident energies up to 0.90 GeV the data evolve systematically, in accord with lower-energy results. However, above this energy, the spectra at intermediate and backward angles indicate a distinctively different character which appears to be nearly independent of bombarding energy.

Another aspect of the energy spectra that suggests a mechanism change above 0.90 GeV is found in the behavior of the Coulomb peaks [33,34]. At 0.90 GeV and below, the Coulomb peaks and widths at a given angle show little dependence on bombarding energy. Above this value, however, the most probable energy decreases systematically and the width of the Coulomb peak increases, extending the spectra down to significantly lower fragment energies relative to spectra at 0.90 GeV and below. That this behavior is not due to simple kinematic shifts is indicated by the existence of this same effect in both forward- and backward-angle spectra. This result is consistent with a mechanism in which the Coulomb field of the emitting system is strongly modified, e.g., by expansion of the source [22] and/or by multiple charged-particle emission either prior to or simultaneous with the fragment in question. Similar changes in the energy spectra have been reported for the $p$+Xe and $^{12}$C+$^{197}$Au systems [27,12].

Energy spectra for the 1.8-GeV $^3$He+$^{197}$Au system are shown in Fig. 5 for $Z=4$–9 spectra observed at 60° from

TABLE I. Differential (mb/sr) and total (mb) cross sections for 0.90- and 3.6-GeV $^3$He+$^{nat}$Ag reactions as a function of fragment charge and laboratory emission angle.

| | 0.90 GeV | | | | | 3.6 GeV | | | | |
|---|---|---|---|---|---|---|---|---|---|---|
| $\theta^{lab}$ | 25° | 63° | 107° | 149° | total | 25° | 63° | 107° | 149° | total |
| $Z$ | | | | | | | | | | |
| 3 | 9.6 | 6.7 | 3.5 | 2.5 | 64 | 33 | 27 | 13 | 11 | 250 |
| 4 | 2.5 | 1.7 | 1.5 | 0.81 | 19 | 12 | 13 | 11 | 7.3 | 140 |
| 5 | 2.0 | 1.1 | 0.59 | 0.45 | 12 | 12 | 8.0 | 4.8 | 4.2 | 83 |
| 6 | 1.4 | 0.79 | 0.50 | 0.44 | 8.8 | 9.9 | 8.1 | 4.0 | 3.4 | 75 |
| 7 | 0.6 | 0.55 | 0.26 | 0.20 | 4.9 | 5.1 | 3.9 | 1.9 | 1.7 | 37 |
| 8 | 0.48 | 0.34 | 0.19 | 0.11 | 3.3 | 3.7 | 3.4 | 1.4 | 1.1 | 29 |
| 9 | 0.28 | 0.20 | 0.081 | 0.045 | 1.7 | 2.1 | 1.8 | 0.73 | 0.52 | 14 |
| 10 | 0.35 | 0.20 | 0.070 | 0.065 | 1.9 | 2.5 | 2.1 | 0.61 | 0.65 | 17 |
| 11 | 0.38 | 0.18 | 0.041 | 0.039 | 1.6 | 2.4 | 1.8 | 0.46 | 0.52 | 15 |

the $^3$He+$^{197}$Au reaction. The transition from a Maxwellian shape to a Gaussian-like shape [16,39] with increasing $Z$ is quite evident. Spectra at other energies and angles exhibit similar trends.

In order to investigate the velocity of the emitting source, rapidity plots for carbon fragments from the 0.90- and 3.6-GeV bombardments of $^{nat}$Ag are shown in Fig. 6. Invariant cross sections are plotted on a grid of velocity perpendicular to the beam versus velocity parallel to the beam. The source velocities for the 0.90-GeV bombardment range from 0.4 to 0.6 cm/ns, with the Coulomb peak described by a single source of velocity of about 0.4 cm/ns. The higher-kinetic-energy fragments appear to originate from sources with higher velocities. Similar results have been reported earlier for the $p+^{nat}$Ag system [31]. The source velocities for the 3.6-GeV data extend over a much greater range from 0.07 cm/ns for IMF's with energies below the Coulomb peak to 0.7 cm/ns for the energetic tail. These can be described empirically by a linear relationship $v_{\parallel}$ (source) $\cong 0.20 v_{IMF} - 0.25$, where $v$ is the IMF velocity in cm/ns. Thus the Coulomb peaks of the distribution appear to originate from a source of much lower velocity at 3.6 GeV than at 0.90 GeV. However, the most energetic fragments correspond to sources with similar velocities at both bombarding energies. The implication of this result is that the more energetic IMF's originate from more rapidly moving sources, e.g., higher deposition energies or some subset of nucleons moving within the nuclear volume. This is consistent with a nonequilibrium emission mechanism. However, when multiple IMF emission is observed, this pattern is altered, as discussed in Sec. IV.

Elemental yield distributions for the $^3$He+$^{nat}$Ag and $^{197}$Au systems also undergo a change in character above 0.90 GeV. A power-law fit to the charge distribution data, $\sigma(Z) \propto Z^{-\tau}$, has been performed at each energy and angle, as well as for the total yield, as shown in Fig. 7. A power-law distribution has been predicted by the theory of condensation near a critical point developed by Fischer [40] and applied to IMF data in Refs. [26–29]. The power-law exponent in this theory is predicted to have a minimum at $\tau \approx 2$ near the critical point, consistent with the high-energy results obtained here. However, similar behavior is also predicted by several models, e.g., statistical multifragmentation, percolation, and cold-cracking theories [19–23]. The present data do not permit

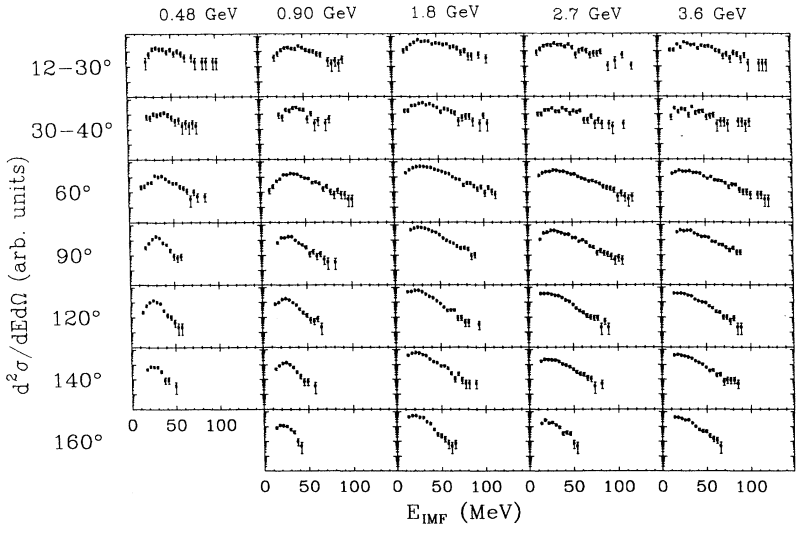


FIG. 2. Carbon fragment energy spectra for the $^3$He+$^{nat}$Ag reaction at 0.48, 0.9, 1.8, 2.7, and 3.6 GeV over the angular range 12°–160°.

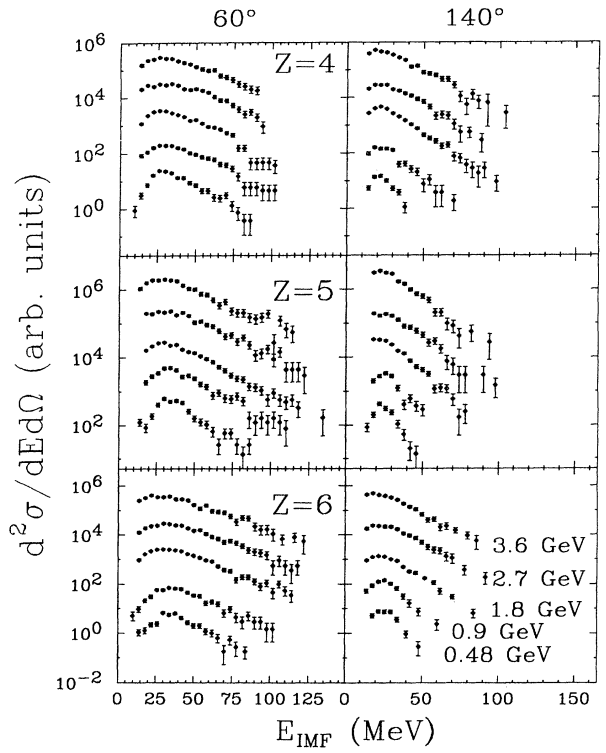


FIG. 3. Energy spectra for $Z=4$, 5, and 6 fragments observed in the $^3He+^{nat}Ag$ reaction at 60° and 140° for bombarding energies of 0.48 (bottom), 0.9, 1.8, 2.7, and 3.6 (top) GeV.

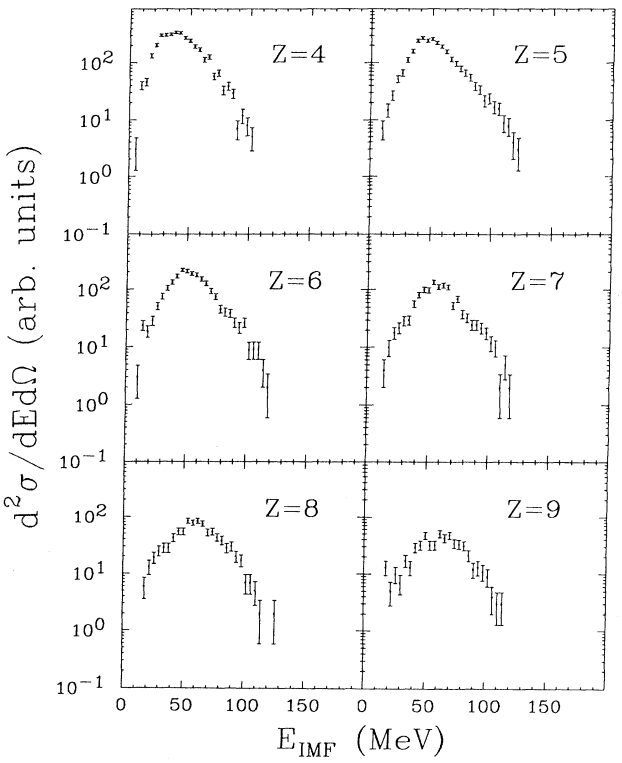


FIG. 5. Energy spectra for $Z=4$–9 fragments from the reaction of 1.8-GeV $^3He$ ions with $^{197}Au$ ions observed at 60°.

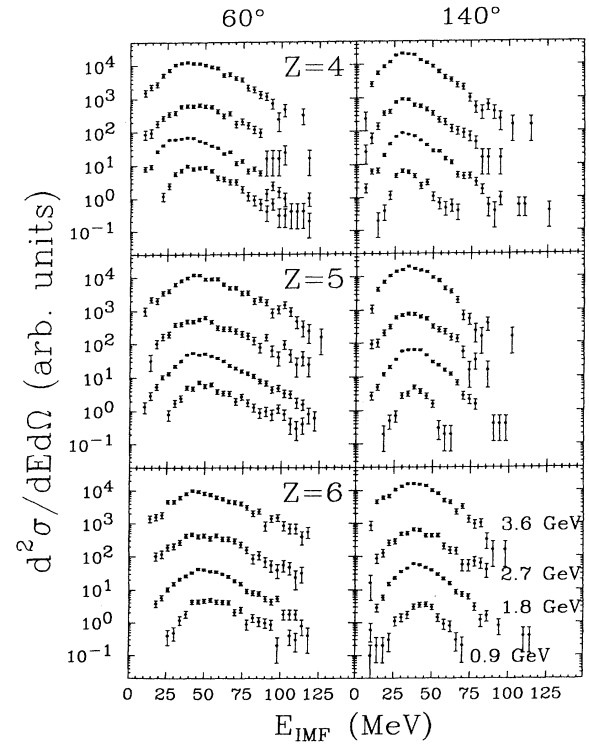


FIG. 4. Energy spectra for $Z=4$, 5, and 6 fragments observed in the $^3He+^{197}Au$ reaction at 60° and 140° for bombarding energies of 0.9 (bottom), 1.8, 2.7, and 3.6 (top) GeV.

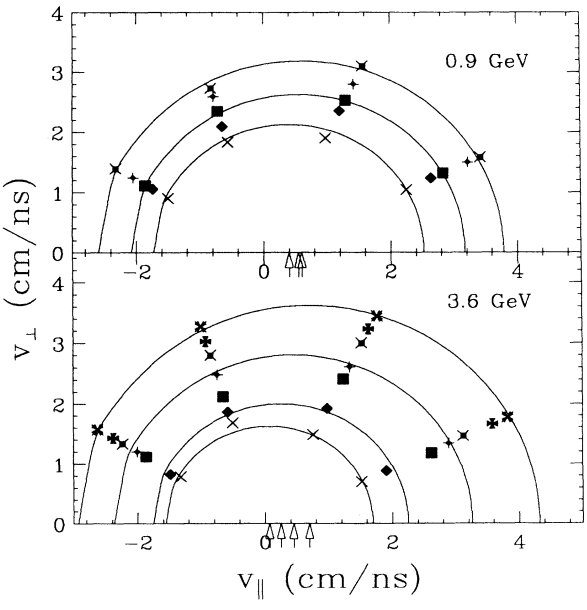


FIG. 6. Plot of longitudinal velocity $v_\parallel$ versus perpendicular velocity $v_\perp$ for carbon emitted at 0.9 (upper) and 3.6 (lower) GeV for the $^3He+^{nat}Ag$ inclusive data. Arrows on the abscissa indicate source velocity for each invariant cross-section ring.

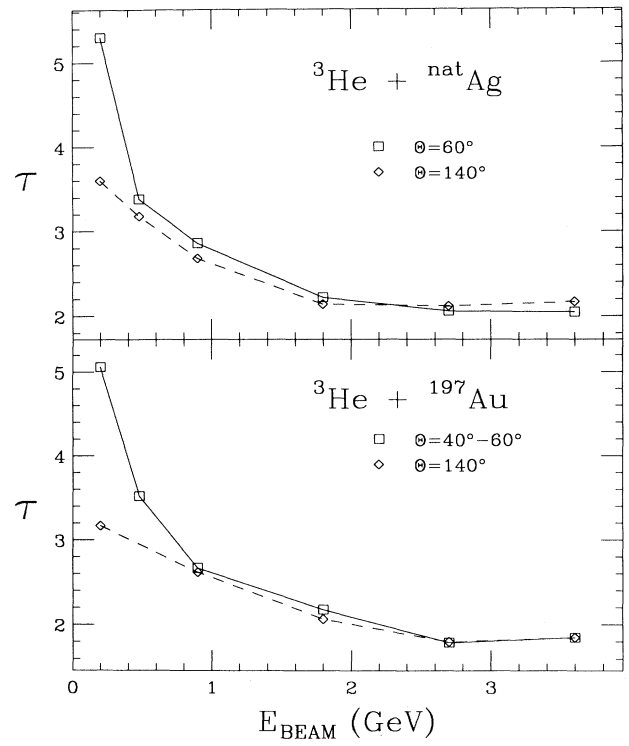


FIG. 7. Power-law parameter $\tau$ as a function of bombarding energy for $^{nat}$Ag and $^{197}$Au targets. Data at 0.20 GeV are from Ref. [16].

differentiation among these theories.

At a minimum, changes in the behavior of $\tau$ may indicate a change in reaction mechanism [41,42]. This has been previously demonstrated for the $^3$He+$^{nat}$Ag system at 200 MeV [16], where a strong difference is observed in the $\tau$ parameters at forward angles (characterized by a nonequilibrium decay mechanism) and at backward angles (where the spectra are consistent with emission from an equilibrated source). These differences are apparent in Fig. 7, where the 200-MeV results are included. The dependence of $\tau$ on bombarding energy shows a smooth decrease with incident energy at both forward and backward angles up to 1.8 GeV, after which the power-law exponent becomes essentially constant at $\tau=2.1\pm0.1$ for $^{nat}$Ag and $1.9\pm0.1$ for $^{197}$Au. This saturation of the $\tau$ parameter has also been seen in proton-induced reactions [27,35]. However, for the $^{197}$Au system, the minimum is not fully achieved until 2.7 GeV, as opposed to 1.8 GeV for the $^{nat}$Ag system. This is consistent with the energy spectra, where the high-energy tails become constant at or above 2.7 GeV for the $^{197}$Au system and 1.8 GeV for the $^{nat}$Ag system. This may reflect the greater "heat sink" of a larger nucleus, as the total binding energy is 65% greater for $^{197}$Au than for $^{nat}$Ag.

## IV. COINCIDENCE STUDIES

The inclusive studies discussed above have indicated a reaction mechanism change above 1 GeV of bombarding energy, prompting the coincidence studies on $^{nat}$Ag described in Sec. II. In Fig. 8 we show the differential cross sections as a function of observed coincidences, $M^{obs}_{IMF}$, for IMF's directly measured in this work. The range of IMF charge acceptance is $Z=3-12$. Calculations of the probability for false multiplicities due to multiple interactions in the target indicate that for multiplicity $M=4$ this effect should account for less than 5% of the events. For $M=5$, however, this uncertainty is a factor of 2, and therefore these events were not included in the subsequent analysis.

At both energies the evidence for multifragment emission is clear. In addition to the significant increase in the total probability for multifragment emission at the higher energy, there is a strong enhancement in the cross section as a function of multiplicity at 3.6 GeV relative to 0.90 GeV. For example, the differential cross section for $M^{obs}_{IMF}=3$ events is over 40 times larger at 3.6 GeV than at 0.9 GeV.

In an effort to assess the effects of detector geometrical acceptance on the observed coincidence distributions, base-line Monte Carlo simulations have been performed.

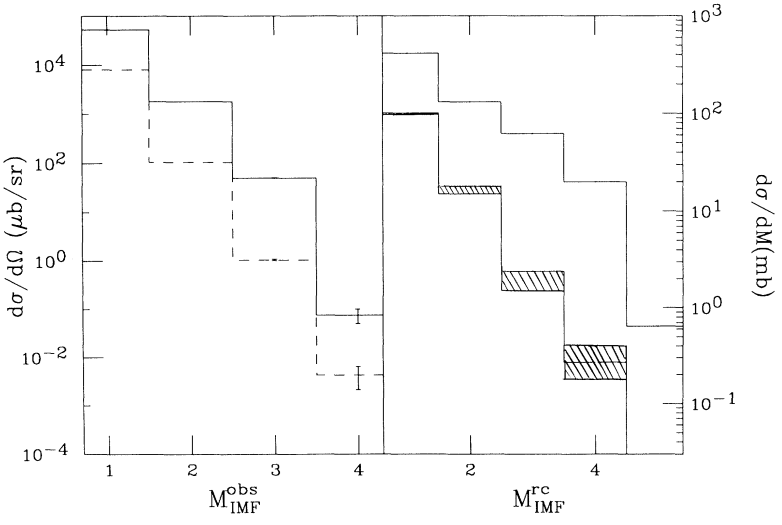


FIG. 8. Left: differential IMF cross sections as a function of multiplicity for observed multifragment events measured in the $^3$He+$^{nat}$Ag reaction at 0.9 GeV (dashed line) and 3.6 GeV (solid line); errors are statistical. Right: Monte Carlo reconstruction of data to account for detector geometry. Upper line shows results for 3.6 GeV, which assumes singles angular distribution. Lower line is for 0.90 GeV; the crosshatched area indicates effects of including angular distribution assumptions and statistics, as discussed in text.

In this simulation the Monte Carlo input was adjusted until the filtered output matched the observed data. No energy cuts were included, only geometric acceptance. The simulations included two different assumptions: (1) experimental angular distributions corresponding to the inclusive IMF yields and (2) an isotropic emission pattern. The values of the reconstructed coincidence distribution $M_{\mathrm{IMF}}^{\mathrm{rc}}$ are also shown in Fig. 8 for the data at 0.90 GeV, where these two assumptions diverge most noticeably. The effect is found to be relatively small. Thus these values should provide approximate *lower* limits for the true multiplicity distributions. The reconstructed distributions yield minimum cross sections for multifragment events ($M \geq 2$) of about 220 mb at 3.6 GeV and 20 mb at 0.9 GeV.

In the left frame of Fig. 9, we show the summed IMF charge distributions for multiple IMF events, $M_{\mathrm{IMF}}^{\mathrm{obs}} \geq 2$. Light-charged particles (H and He) are not included in these sums. At 3.6 GeV bombarding energy, events are detected which account for up to 75% of the total available charge. Figure 9 demonstrates that the observed multifragment products contain significant contributions from higher-$Z$ fragments and are not exclusively due to light elements such as Li and Be.

In the right frame of Fig. 9, the total observed kinetic energy per event is shown for $M_{\mathrm{IMF}}^{\mathrm{obs}} \geq 2$. This sum extends up to 400 MeV, again with light-charged particles excluded. The solid line in this plot is the result of a calculation based upon sequential statistical emission of IMF's from an equilibrated source, corrected for detector acceptance. The simulation assumed experimental fragment charge distributions and the reconstructed multiplicity results from Fig. 8. Corrections also were included for the velocity of the emitting source, as determined by rapidity plots for the singles data (Fig. 6). In order to maximize fragment kinetic energies, an initial temperature of 8 MeV was assumed and cooling by H and He emission was blocked in the calculation. Thus this calculation should serve as an upper bound on the energies. Even for these extreme assumptions, however, the calculated total kinetic energies fail to approach the experimental distribution, suggesting that the fragment acceleration mechanism is more complex than simple Coulomb repulsion from a thermal source.

Comparison of the summed IMF charge and kinetic energy distributions for $M_{\mathrm{IMF}}^{\mathrm{obs}} \geq 2$ in Fig. 9 reveals qualitatively similar shapes at 0.90 and 3.6 GeV. This is in contrast to the IMF singles data at these two energies, where distinct changes in the charge distribution and energy spectra were noted in Sec. III [35]. We interpret this result as due to the dominance of nonequilibrium processes in the multiplicity-1 IMF yields at 0.90 GeV, whereas at 3.6 GeV there is a much higher relative probability for multifragment emission.

Figure 10 shows the correlation angle of fragments observed in the 32-element global array in coincidence with trigger detectors at 25°, 63°, 107°, and 149° in the planar array. Here the ratio of fragments emitted on the opposite side of the beam ($O$) to those on the same side ($S$) in the array, $O/S$, is plotted as a function of trigger angle. A value near $O/S = 1$ would imply a random distribution of events.

When the trigger detector is at 25°, there is a strong preference for the partner fragment to be on the opposite side of the beam for the two forward hemisphere rings at 35° and 63°. However, the most backward ring shows little preference for one side or the other. There is also an overall trend in the data for the partner of fragments in the 25° trigger detector to be observed in the backward detectors and vice versa. As the trigger detector is moved toward more backward angles, the preference for emission to the other side of the beam diminishes. For the most backward trigger (149°), there is only about a 20% preference for partners to be observed on the opposite side of the beam. Therefore triggering on IMF's emitted at backward angles seems to select a more random spatial distribution, whereas triggering on an IMF emitted in the forward direction seems to favor those events whose partners have opposing transverse-momentum vectors. This may indicate that backward-emitted IMF's are correlated with a more spherical event shape, consistent with the simultaneous multifragmentation event-shape model discussed in the next subsection.

In the inclusive experiment, power-law fits to the

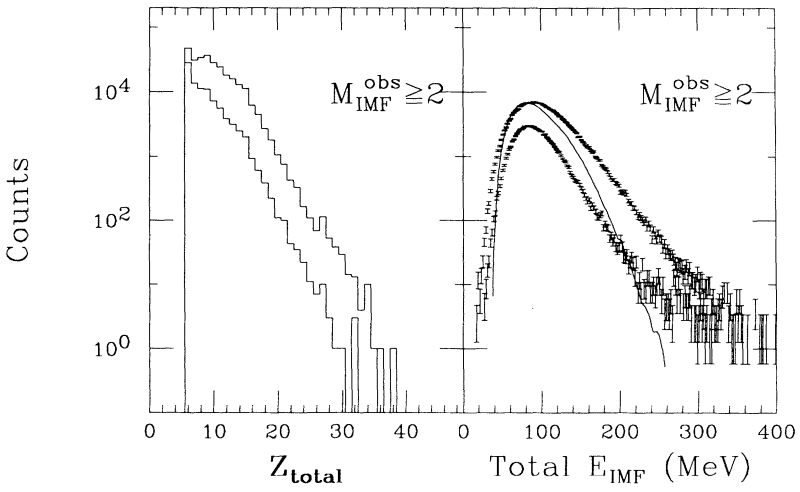


FIG. 9. Left: distributions of the summed IMF charge for IMF's with $M_{\mathrm{IMF}}^{\mathrm{obs}} \geq 2$ for the 3.6- (top) and 0.90- (bottom) GeV $^3$He+$^{\mathrm{nat}}$Ag reactions. Right: distributions of the summed detected kinetic energy per event for IMF's for $M_{\mathrm{IMF}}^{\mathrm{obs}} \geq 2$ for 3.6 (top) and 0.90 (bottom) GeV. Solid line is the result of the calculation described in text.

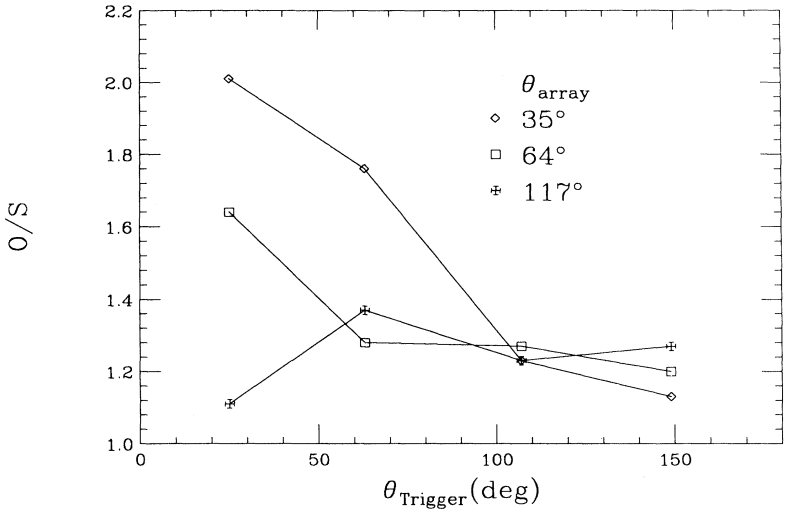


FIG. 10. Ratio of fragments detected in the global array on the opposite side ($O$) of the beam to fragments on the same side ($S$) of the beam when triggered by detectors in a planar array, $\Theta_{trigger}$. Array detector angle $\Theta_{array}$ is indicated in figure.

charge distributions indicated a reaction mechanism change between 0.90 and 1.8 GeV. The left frame of Fig. 11 shows how the power-law parameter $\tau$ for a given trigger detector changes as a function of the angle of observation for the $M_{IMF}^{obs} \geq 2$ data at these two energies. The solid line represents the value of $\tau$ obtained from a fit to the total $M_{IMF}^{obs}=2$ charge distributions. Forward-emitted IMF's are found to trigger events with steeper charge distributions, i.e., larger $\tau$ values. As the angle of the trigger detector increases, the $\tau$ value decreases monotonically, especially at 3.6 GeV. The backward-emitted IMF's appear to isolate events where the ratio of coincident heavy fragment to coincident light fragments is larger than for the forward detectors.

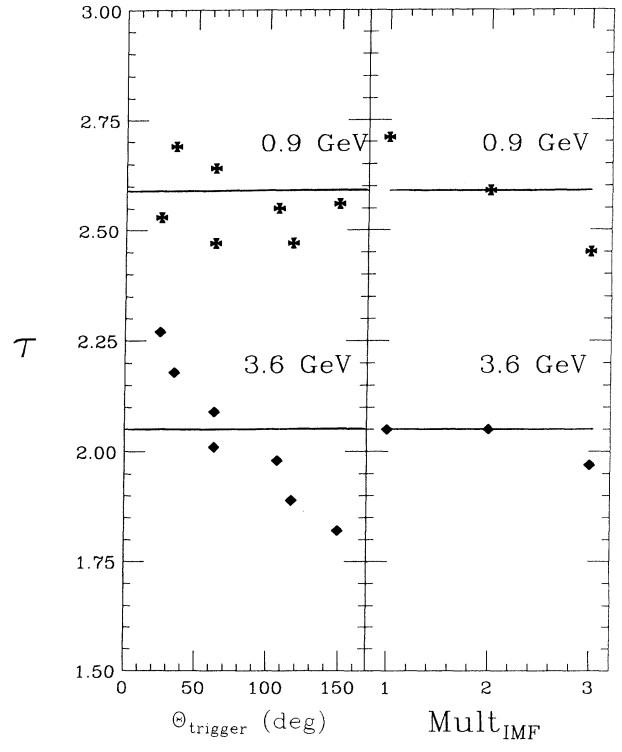


FIG. 11. Power-law exponent $\tau$ as a function of the angle of a coincident trigger detector (left) and different multiplicities of IMF's (right). The solid lines represent the $\tau$ values for multiplicity=2.

The right frame of Fig. 11 shows how the average $\tau$ parameter changes as a function of IMF multiplicity. For the 3.6-GeV data, there is very little dependence on the multiplicity of the trigger. For the 0.90-GeV data, $\tau$ decreases as the multiplicity of the trigger increases. In the lower-energy case, there is a high probability that most $M=1$ events are true "binary" processes, for which $\tau$ values are usually larger than for multifragment events. At 3.6 GeV, however, many of the observed singles are really higher-multiplicity events for which the partner has not been detected due to our low solid-angle coverage. Thus triggering on the higher observed multiplicity does not significantly change $\tau$ at the higher energy.

One of the most interesting pieces of evidence for a reaction mechanism change in the inclusive data was the change in spectral shape at higher bombarding energies. In Fig. 12 we show spectra for $Z=6$ fragments when different IMF multiplicities are used as a trigger. At an angle of 117°, there is a marked flattening of the slope of the high-energy tails for the higher multiplicities. A simple Maxwellian fit to the laboratory spectra at 3.6 GeV yields slope parameters of $T=13$, 15, and 19 MeV for $M_{IMF}^{obs}=1$, 2, and 3, respectively. As the angle of observation moves to more forward angles, these differences become less pronounced. Also evident in the data is the characteristic broadening of the Coulomb peaks as the multiplicity of the trigger increases. Higher-multiplicity events extend the Coulomb peak to lower energies and produce a larger high-energy tail relative to singles events. These features are similar to those predicted by the expanding-evaporating source model of Friedman [22]; i.e., very energetic fragments are emitted early in the expansion and low-energy fragments originate from the expanded nucleon gas. Figure 13 shows the change in energy spectra at 117° with multiplicity for a variety of fragment charges observed at 3.6 GeV. The same behavior of the energy spectra is observed as in Fig. 12, i.e., a

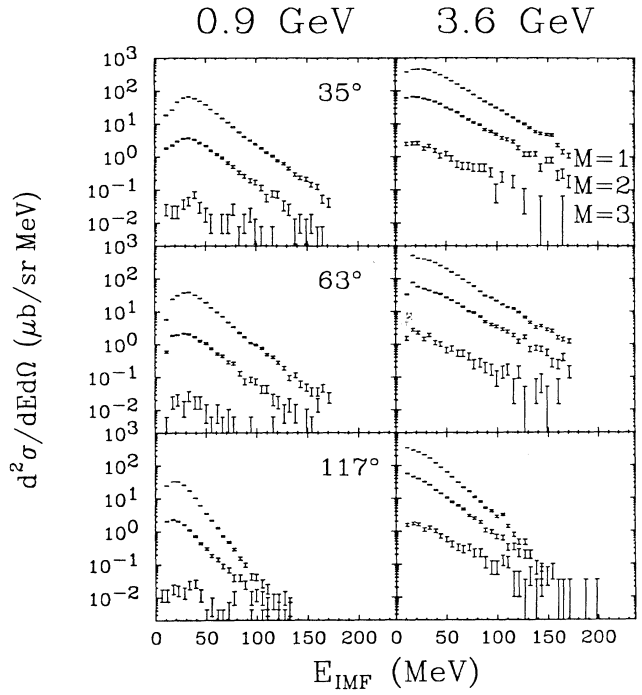


FIG. 12. Energy spectra for carbon fragments measured in the $^3He+^{nat}Ag$ reaction at 0.9 GeV (left column) and 3.6 GeV (right column) gated on fragments emitted at 35° (top row), 63° (middle row), and 117° (bottom row). For each frame the spectra are gated on multiplicity, as shown on figure.

broadening and shifting of the Coulomb peaks, as well as a hardening of the high-energy tails, as a function of increasing multiplicity.

Another perspective on the influence of multiplicity on reaction observables is illustrated by the rapidity plots shown in Fig. 14 for carbon fragments emitted in the 3.6-GeV bombardment. For $M_{IMF}^{obs}=1$ (top), the source velocity appears to increase approximately linearly from $v_s \approx 0.4$ to 0.8 cm/ns as a function of IMF velocity, as discussed in Sec. III. Similar results have also been noted in previous inclusive studies [31]. In contrast, for $M_{IMF}^{obs}=3$ (bottom), all the data are well described by a single-source velocity $v_s \approx 0.4$ cm/ns. The relatively low source velocity for these high-multiplicity (and implicitly more violent) events suggests that the energy dissipation process involves large transverse-momentum transfer. For example, $v_s=0.4$ cm/ns corresponds to a complete fusion process involving a 200-MeV $^3He$ ion; however, at such a low excitation energy, the probability for $M_{IMF}>1$ events is small.

The combined behavior of Figs. 12–14 argues against a sequential IMF emission mechanism. The low source velocities and very high spectral slope temperatures—i.e., $T \simeq 19$ MeV for laboratory spectra at backward angles—are incompatible with a large deposition energy event that emits fragments stepwise.

## V. DISCUSSION OF RESULTS

Two underlying questions concerning fragmentation phenomena are (1) what are the dynamics of energy dissipation in the collision state, and (2) on what time scale does the disassembly of hot nuclei occur? The excitation of complex nuclei to high internal energies in light-ion-induced reactions cannot be readily accounted for by simple nucleon-nucleon scattering processes [43–45]. Since the threshold for multifragmentation is estimated to be about $E^*/A \gtrsim 4$–5 MeV [46,47], an efficient mechanism for rapid energy dissipation must be identified. As shown in Fig. 1, the probability for IMF emission increases rapidly with bombarding energy—nearly three orders of magnitude between 90 MeV and 3.6 GeV. At the same time, the increase in the average excitation energy over corresponding energy interval is less than a factor of 3, as deduced from linear-momentum transfer systematics

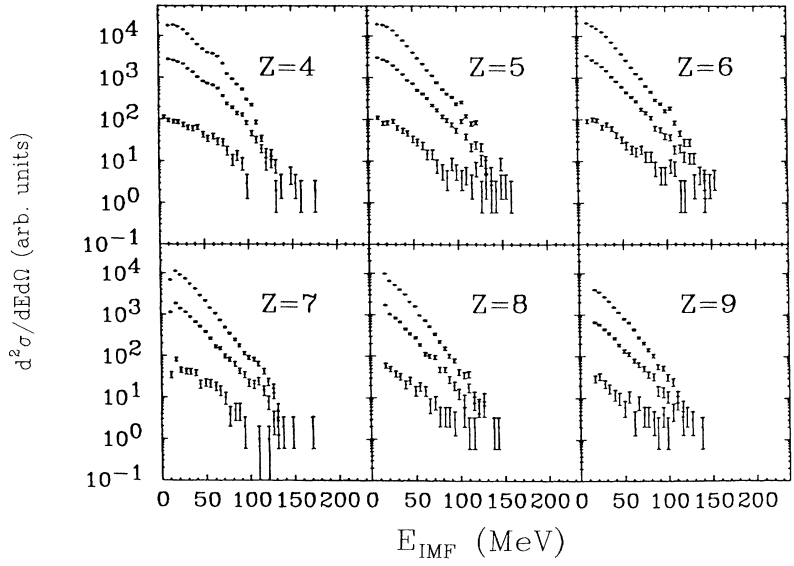


FIG. 13. Energy spectra for $Z=4$–10 fragments emitted at 117° from the 3.6-GeV $^3He+^{nat}Ag$ reaction. Multiplicity gates are $M=1$ (top), $M=2$ (middle), and $M=3$ (bottom).

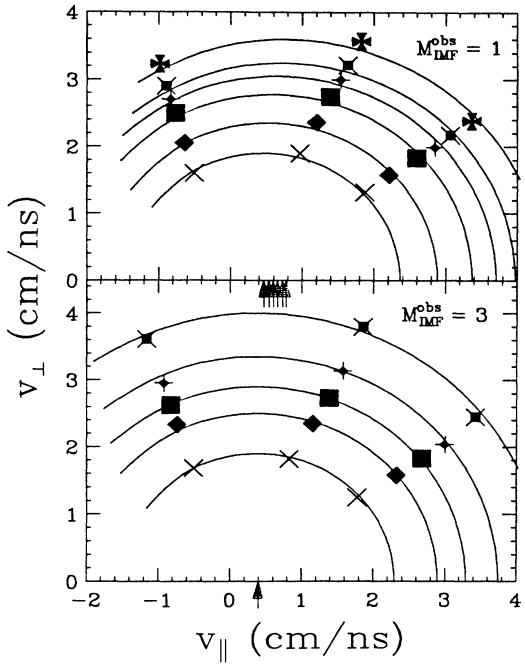


FIG. 14. Invariant cross sections for carbon fragments produced in the 3.6-GeV $^3$He+$^{nat}$Ag reaction. Top: fragments gated on $M_{IMF}^{obs}=1$; arrows are source velocity centroids of best-fit contour lines through the data; increasing centroids correspond sequentially to contour lines. Bottom: fragments gated on $M_{IMF}^{obs}=3$; arrow is source-velocity centroid for all contour lines.

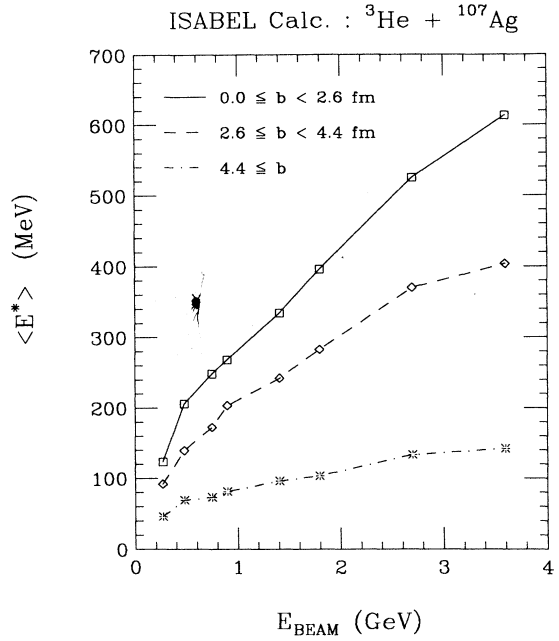


FIG. 15. Average excitation energy in the nucleus after initial nuclear cascade as predicted by ISABEL intranuclear cascade code [43], as a function of bombarding energy. Different impact parameters $b$ are indicated in figure.

[48–50] and intranuclear cascade calculations [43–45].

In order to estimate the range of excitation energies and temperatures associated with these $^3$He+$^{nat}$Ag results, the ISABEL intranuclear cascade code [43] has been run for a full range of impact parameters $b$ as a function of $^3$He bombarding energy. These calculations, shown in Fig. 15, indicate that for the total reaction cross section, the increase in the excitation energy $E^*$ of the residual nuclei is a relatively weak function of bombarding energy. However, for central collisions (defined here as $b \leq 2.6$ fm), the average excitation energy increases rapidly with bombarding energy. The limit of stability against multifragmentation is predicted by several theories [21,22,26] to be in the vicinity of 500 MeV excitation energy. For the 3.6-GeV $^3$He+$^{nat}$Ag reaction, the ISABEL calculation (Fig. 15) predicts across section of approximately 400 mb for events with excitation energies in excess of 500 MeV. This is to be compared with a cross section of 200 mb for multifragment events reported here.

The growth in average excitation energy shown for central collisions in Fig. 15 can be related to the increasing probability for Δ production as a function of bombarding energy. Excitation of the Δ resonance, followed by rescattering, isotropic decay, and pion reabsorption, provides an efficient mechanism for large energy dissipation on a fast time scale and significant transverse-momentum transfer. This possible correlation is supported by the changes in reaction observables for the present data between $E/A=300$ and 600 MeV, the energy region in which the cross section for Δ production in $N$-$N$ collisions grows rapidly. Cugnon, Mizutani, and Vandermuellen [44] have estimated that, at $E/A=700$ MeV, about 50% of primary $N$-$N$ collisions result in Δ formation. In addition, Campi *et al.* [51] have reported that in central collisions the number of $N$-$N$ collisions can be correlated with the number of fragments produced. All of these arguments suggest that the Δ resonance plays an important role in fragmentation processes in light-ion collisions.

The question of time scales must also be addressed. Is multifragment emission an "instantaneous" process where the nucleus breaks up into several fragments on a time scale comparable to the collision time? Or does it occur via an extended series of statistical binary decays leading to a similar multifragment final state? Or is it some intermediate process?

One of the expected differences between sequential decay and more rapid processes is the event shape, i.e., the pattern of fragment momentum vectors that represents the average event. A simultaneous breakup should result in a more spherical event shape, whereas a sequential decay should produce a more elongated spheroidal pattern [52,53]. Since reactions probably occur on a distribution of time scales, separation into these two extremes is a simplification of the real situation [45].

Lopez and Randrup [52] have performed a calculation comparing the kinematical differences between a sequential and a simultaneous fragmentation mechanism. This analysis is applied to the 3.6-GeV data for each event of $M \geq 3$ observed in this work. A kinetic flow tensor is defined, which can then be used to determine sphericity $S$ and coplanarity $C$ shape parameters. The parameters

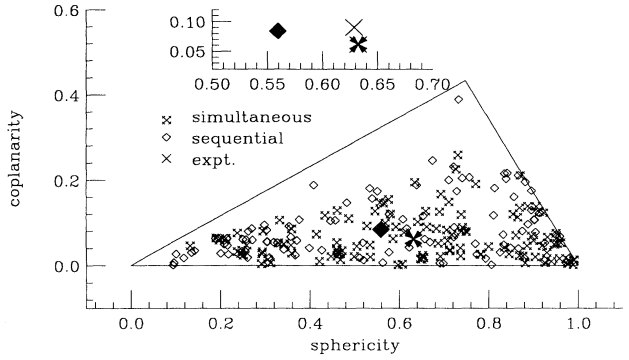


FIG. 16. Theoretical prediction of event shape for a simultaneous multifragmentation and a sequential multifragmentation, filtered through our experimental geometry. The centroids of the simultaneous calculation, sequential calculation, and experimental data distributions are shown in the inset.

show characteristic patterns, depending on the decay kinematics. A sphericity versus coplanarity analysis of the 3.6-GeV data is shown in Fig. 16. The centroids of the experimental distribution are $S=0.63$ and $C=0.090$.

In order to compare these experimental coordinates with theoretical predictions, both the center-of-mass motion of the system and the detector acceptance must be taken into account. The Lopez-Randrup calculation [52] was run for this case using a nuclear density of 0.02 and the output filtered through the detector system. The centroid of the simultaneous fragmentation distribution is predicted to be $S=0.63$, $C=0.06$, while the centroid of the sequential fragmentation distribution is $S=0.56$, $C=0.06$. The inset of Fig. 16 compares the centroids of these distributions with the experimental data. The sphericity of the data coincides with the simultaneous sphericity; however, there is a discrepancy in the coplanarity. The experimental event-shape centroid looks slightly more disklike than the simultaneous prediction. Since this experiment sampled only 8% of the total solid angle, this conclusion must be interpreted with caution.

Compared with the data of Cebra *et al.* [53] for the $^{40}Ar+^{51}V$ reaction at $E/A=35-85$ MeV, which had centroids of approximately $S=0.3$, $C=0.14$, the current data set looks more spherical. A large part of the difference in the sphericity is due to the fact that heavy-ion-induced reactions focus fragments in the beam direction, causing more rodlike events relative to light-ion-induced reactions.

In order to investigate the possibility that these higher-multiplicity events are a result of multiple binary breakups, the GEMINI [55] code for IMF evaporation has also been run. Extracting our starting point from the average excitation energy for central collisions predicted by the INC code (Fig. 15), we ran a system at 610 MeV excitation energy with $l_{max}=76\hbar$. These values were chosen to provide an upper limit for sequential decay. This angular momentum coincides with an impact parameter of 2.6 fm with a bombarding energy of 3.6 GeV and is well in excess of the limiting angular momentum of this system [56]. Thus the calculation should produce enhanced IMF yields relative to more realistic assumptions. The cross sections as a function of fragment charge are shown in Fig. 17, along with the experimental data. The calculation severely underpredicts the experimental cross sections, both in relative yields and absolute magnitude. Figure 18 shows the calculated multiplicity of IMF's from GEMINI in comparison with the experimentally measured multiplicity, corrected for detector acceptance and angular distribution. In both distributions the singles events dominate, but are underpredicted by the calculation. The discrepancy between the data and calculation increases as the multiplicity increases. The average multiplicity as predicted from GEMINI for IMF's is 1.02 as compared with the experimental value of 1.07. The results imply that either sequential multifragmentation is inconsistent with the data or the physics contained in the GEMINI code is inadequate to deal with these very-high-excitation-energy events.

In an effort to account for both the reaction dynamics and the subsequent fragmentation stage, Cugnon and Volant have performed calculations which couple the intranuclear cascade code dynamics with a percolation model [20] for generating complex fragments [57]. Here their model is applied to the results of the $^{3}He+^{nat}Ag$ reaction. The INC code of Cugnon *et al.* is employed to describe the energy dissipation stage of the reaction [44,45]. In these calculations the cascade is stopped after 30 fm/$c$, at which time the percolation procedure is applied to the expanded, excited matter distribution predicted by the code. The calculations are normalized to a total cross section of 2.0 b, predicted [58] using a radius

$$R=1.04A_p^{1/3}+1.12A_T^{1/3}+1.2 \text{ fm} .$$

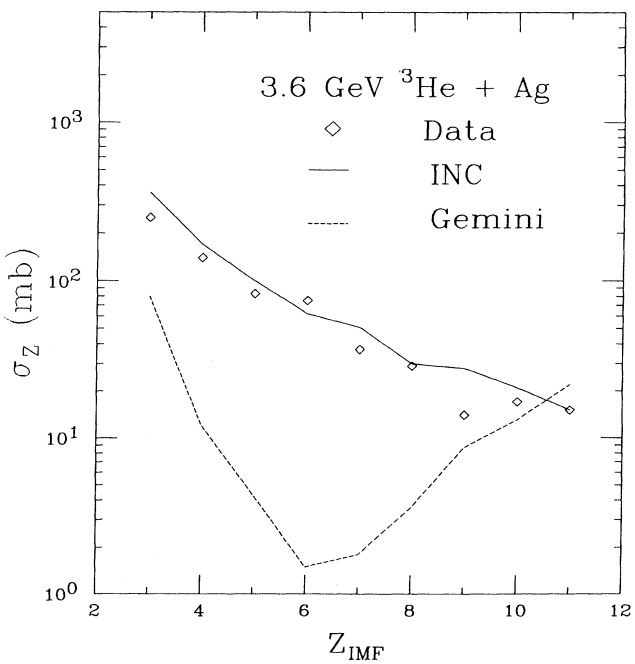


FIG. 17. Charge distribution of IMF's as predicted by the GEMINI code [55] (dashed line) and INC/percolation calculation [57] (solid line), compared with experimental data at 3.6 GeV.

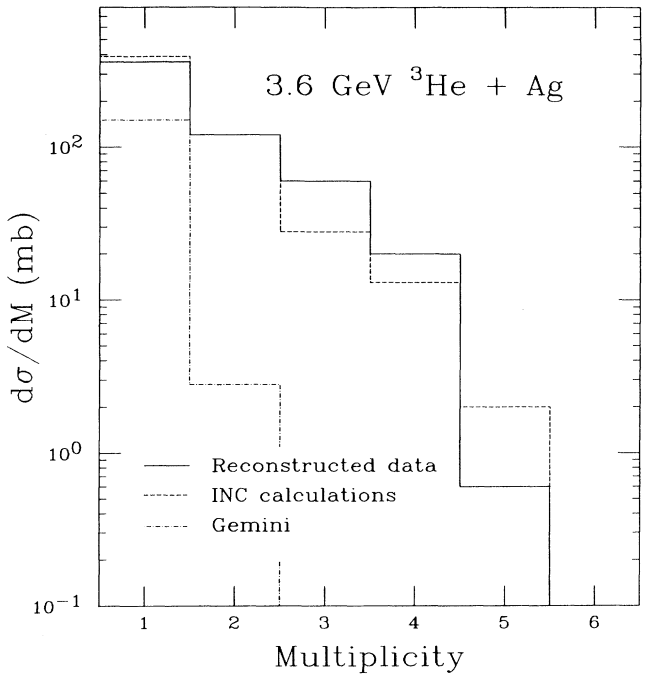


FIG. 18. Multiplicity prediction for GEMINI [55] (dot-dashed line) and INC/percolation calculation [57] (dashed line), compared with the 3.6-GeV data (solid line).

The percolation assumes that two nucleons belong to the same cluster if their relative distance at the time the INC distribution is frozen is smaller than some percolation distance $d_c$. Here $d_c$ is taken as 2.0 fm. Previous calculations with this model have achieved moderate success in describing both proton- and heavy-ion-induced reactions [57]. One deficiency of the present version of the code is that Coulomb repulsion is not taken into account. Therefore we cannot compare with energy spectra.

In Fig. 17 the percolation calculations for the IMF charge distribution for the 3.6-GeV $^3$He+$^{nat}$Ag reaction are compared with the data. Figure 19 shows the parameter $\tau$ derived from fitting a power law to the calculated charge distributions for all measured bombarding energies. In both cases the calculation reproduces the data successfully. However, similar comparisons (not shown) with data from the $^3$He+$^{197}$Au system are less satisfactory, a result that may be partially due to the contributions of very asymmetric fission events to the measured charge distributions.

Figure 18 shows the multiplicities predicted by the INC/percolation approach. The agreement is generally within a factor of 2 for each multiplicity. It should be stressed that these calculations were performed without imposing any experimental energy threshold. Introducing such thresholds will reduce the predicted multiplicities, although not to the level of the evaporation treatment. However, if Coulomb repulsion is included in the calculations, multiplicities will increase. While the INC/percolation approach requires more quantitative examination, it represents a significant advance over previous calculations which make arbitrary assumptions about the initial reaction dynamics.

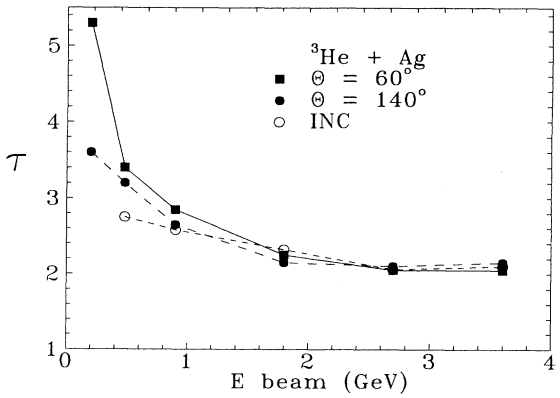


FIG. 19. Comparison of $\tau$ parameters calculated with INC/percolation code [57] with data for the $^3$He+$^{nat}$Ag system.

## VI. CONCLUSIONS

The inclusive data presented here indicate a reaction mechanism change between 0.90 and 1.8 GeV in the $^3$He+$^{nat}$Ag system and near 1.8 GeV in the $^3$He+$^{197}$Au system. This conclusion is supported by (1) fragment energy spectra at backward angles that undergo a significant change in the slope of the high-energy tails above 0.90 GeV; (2) spectral Coulomb peaks that broaden and shift to lower energies in this same energy region; (3) an increase in the cross section for IMF's as a function of bombarding energy—especially at backward angles—that is much stronger than the increase in the average excitation energy predicted by the intranuclear cascade calculation or linear-momentum transfer systematics; and (4) attainment of a constant minimum in the power-law parameter $\tau$, which describes the charge distributions at bombarding energies $E \geq 1.8$ GeV for the $^{nat}$Ag system and $E \geq 2.7$ GeV for the $^{197}$Au system.

The energy spectra provide valuable insight into the underlying physics. As the bombarding energy increases, the broadening of the Coulomb peaks toward lower energies suggests that fragment separation occurs from a distribution of charge centers. Multiple charged-particle emission either prior to or simultaneous with the detected fragment and/or emission from an expanded source are possible explanations for this behavior. The enhancement of the high-energy tails, especially at backward angles, indicates a reaction mechanism that is capable of ejecting high-momentum fragments at all angles.

In the coincidence studies of the $^3$He+$^{nat}$Ag reaction, we have detected multifragment events with multiplicity up to $M=4$ for IMF's, confirming that the change in reaction observables in the inclusive data is associated with the onset of multifragment emission. The probability of high-multiplicity events increases about 40-fold between 0.90 and 3.6 GeV. For some events, up to 75% of the total charge of the system has been detected. Triggering on an IMF emitted at backward angles seems to isolate the more violent events, as evidenced by significant changes in the energy spectra, higher average multiplicities, more random correlation between coincident fragments, and a higher probability for heavier fragments. The energy

spectra exhibit a distinct evolution in shape as the multiplicity increases, especially at backward angles.

A sequential multifragmentation picture, as described by the GEMINI [35] code, seems to be inconsistent with the data, or this current statistical decay code is inadequate to deal with these very-high-excitation-energy events. Moderate success is found with an INC/percolation calculation; there is good agreement with the charge distributions, and a satisfactory description of the fragment multiplicities also results. However, present calculations need to be improved to compare with spectra. Although one must be careful in interpreting the event-shape analysis with only 8% of $4\pi$ detector average, when the event output is filtered through our detector system, the sphericity is the same as that predicted by the simultaneous multifragmentation calculation.

Two qualitative features seem to be essential to explain these data. First, a rapid, efficient energy dissipation mechanism is required to convert projectile kinetic energy into internal excitation energy while at the same time producing a low average source velocity; i.e., the transverse-momentum transfer must be large. One such mechanism is pion production and capture via the excitation and subsequent isotropic decay of $\Delta$ resonances [44]. Such processes occur on a fast time scale ( $\sim 10$ fm/$c$) and provide efficient energy conversion via the pion mass energy and its short mean free path. For central collisions, pion reabsorption is a significant contribution in the $\Delta$ decay channel [45,59], providing an efficient energy damping mechanism with a significant transverse-momentum component due to the kinematics of hard $N$-$N$ scattering and the $NN \rightarrow \Delta N$ channel, and subsequent isotropic decay. Recent INC calculations [47] in which delta excitations are suppressed substantiate this conclusion; i.e., the excitation energy distribution is significantly lower without the $\Delta$.

A second ingredient that appears necessary to explain the multiplicity data and the distortions of the fragment kinetic energy spectra is expansion of the emitting source. Although multiple charged-particle emission prior to or simultaneous with IMF emission may also account for the results, we cite the evolution of the inclusive spectra (Figs. 2–4) as evidence against such a picture. Other than the cross section, the shapes of the spectra do not change appreciably until one reaches 1.8 GeV bombarding energy (see also Ref. [27]). If one were dealing with a sequential mechanism, a systematic evolution of the spectra would be expected as a function of increasing bombarding energy. The $M=3$ spectra in Figs. 12 and 13 reinforce this argument; i.e., the Coulomb peak has virtually disappeared.

Expansion can be qualitatively understood in the context of percolation calculations [58] or the expanding-evaporating source model of Friedman [22]. In the latter model, multifragmentation is treated in terms of surface statistical emission from a hot, expanding nucleus, driven by thermal pressure. This picture can account for the qualitative behavior of the fragment energy spectra in that (1) highly energetic fragments are emitted early in the expansion and reflect the combined acceleration due to the expansion velocity and the Coulomb field near normal nuclear matter density ($\rho \approx \rho_0$) and (2) very-low-energy fragments are emitted later at very low densities ($\rho \approx 0.3\rho_0$), where the Coulomb field and collective velocity are greatly reduced.

Clearly, both improved calculations and more quantitative data are required to test the above interpretations.

## ACKNOWLEDGMENTS

The IU authors wish to acknowledge the hospitality of Dr. J. Arvieux and the SATURNE staff during our stay at LNS for this experiment. We thank G. Milleret, M. Chamouard, and the SATURNE operations crew for providing excellent beams during our runs; C. Mazur, J. P. Passerieux, and J. Giacometti of CEN Saclay and Bill Lozowski of IUCF for their important roles in making these experiments possible. S. Yasur and Z. Fraenkel made available to us the ISABEL code and Lai Wan Woo and Erin Renshaw assisted with the calculations. One of us (S.J.Y.) acknowledges the fellowship support of Amoco Corp. This work was supported by DAPNIA/SPhN, CEN, Saclay, the U.S. Department of Energy, and the National Science Foundation. This research was sponsored by U.S. DOE Grant No. DE-FG02.88ER.40404.A000 and NSF Grant No. PHY-87-14406.

[1] R. Wolfgang, E. W. Baker, A. A. Caretto, J. B. Cumming, G. Friedlander, and J. Hudis, Phys. Rev. **103**, 394 (1956); A. Caretto *et al.*, *ibid.* **110**, 1130 (1958).

[2] N. A. Perfilov, O. V. Lozhkin, and V. P. Samov, Usp. Fiz. Nauk **70**, 3 (1960) [Sov. Phys. Usp. **3**, 1 (1960)].

[3] V. P. Crespo, J. M. Alexander, and E. K. Hyde, Phys. Rev. **131**, 1765 (1963); R. G. Korteling and E. K. Hyde, *ibid.* **136**, B425 (1964).

[4] J. Hudis, in *Nuclear Chemistry,* edited by L. Yaffe (Academia, New York, 1968), p. 169.

[5] W. G. Lynch, Annu. Rev. Nucl. Sci. **37**, 493 (1987).

[6] B. Jakobsson, G. Jönson, L. Karlsson, V. Kopljar, B. Noren, K. Söderstrom, F. Schussler, E. Monnand, H. Nifenecker, G. Fai, J. P. Bondorf, and K. Sneppen, Nucl. Phys. **A509**, 195 (1990).

[7] A. I. Warwick *et al.*, Phys. Rev. C **27**, 1083 (1983).

[8] Y. Kim *et al.*, Phys. Rev. Lett. **63**, 494 (1989).

[9] J. B. Natowitz *et al.*, Nucl. Phys. **A538**, 263c (1992).

[10] J. Peter *et al.*, Nucl. Phys. **A538**, 75c (1992).

[11] S. J. Yennello, E. C. Pollacco, K. Kwiatkowski, C. Volant, R. Dayras, Y. Cassagnou, R. Legrain, E. Norbeck, V. E. Viola, J. L. Wile, and N. R. Yoder, Phys. Rev. Lett. **67**, 671 (1991).

[12] W. Trautman *et al.*, Nucl. Phys. **A538**, 473c (1992).

[13] W. A. Friedman, Phys. Rev. C **40**, 2055 (1989).

[14] M. A. McMahan *et al.*, Phys. Rev. Lett. **54**, 1995 (1985).

[15] J. Gomez del Campo, Phys. Rev. Lett. **61**, 290 (1988).

[16] K. Kwiatkowski, J. Bashkin, H. Karwowski, M. Fatyga,

and V. E. Viola, Phys. Lett. B **171**, 41 (1986).
[17] G. F. Bertsch and Das Gupta, Phys. Rep. **160**, 189 (1988).
[18] C. Gregoire, D. Jacquet, M. Pi, B. Remaud, F. Sebille, E. Suraud, P. Schuck, and L. Vinet, Nucl. Phys. **A471**, 399c (1987).
[19] J. Aichelin, G. Peilert, A. Bohnet, A. Rosenhauer, H. Stöcker, and W. Greiner, Phys. Rev. C **37**, 2451 (1988).
[20] J. Bondorf, R. Donangelo, I. N. Mishustin, C. J. Pethick, H. Schulz, and K. Sneppen, Nucl. Phys. **A443**, 321 (1985).
[21] D. H. E. Gross, Z. Xiao-Ze, and X. Shu-yan, Phys. Rev. Lett. **56**, 1544 (1986).
[22] W. A. Friedman, Phys. Rev. C **42**, 667 (1990).
[23] J. Randrup and S. E. Koonin, Nucl. Phys. **A471**, 355c (1987).
[24] L. G. Sobotka *et al.*, Phys. Rev. Lett. **51**, 2187 (1983).
[25] G. Klotz-Engmann *et al.*, Phys. Lett. B **187**, 245 (1987); Nucl. Phys. **A499**, 392 (1988).
[26] V. V. Avdeichikov *et al.*, Yad. Fiz. **48**, 1736 (1988) [Sov. J. Nucl. Phys. **48**, 1043 (1988)].
[27] N. Porile *et al.*, Phys. Rev. C **39**, 1914 (1989).
[28] M. Mahi *et al.*, Phys. Rev. Lett. **60**, 1936 (1988).
[29] J. E. Finn *et al.*, Phys. Rev. Lett. **49**, 1321 (1982).
[30] R. E. L. Green and R. G. Koretling, Phys. Rev. C **22**, 1594 (1980).
[31] R. E. L. Green, R. G. Korteling, and K. P. Jackson, Phys. Rev. C **29**, 1806 (1984).
[32] A. M. Poskanzer, G. W. Butler, and E. K. Hyde, Phys. Rev. C **3**, 882 (1971).
[33] A. M. Zebelman, A. M. Poskanzer, J. D. Bowman, R. G. Sextro, and V. E. Viola, Phys. Rev. C **11**, 1280 (1975).
[34] G. D. Westfall, R. G. Sextro, A. M. Poskanzer, A. M. Zebelman, G. W. Butler, and E. K. Hyde, Phys. Rev. C **17**, 1368 (1978).
[35] S. J. Yennello *et al.*, Phys. Lett. B **246**, 26 (1990).
[36] H. Quéchon, Ph.D. thesis, Orsay University, 1980.
[37] K. Kwiatkowski, K. Komisarcik, J. L. Wile, S. J. Yennello, D. E. Fields, V. E. Viola, and B. G. Glagola, Nucl. Instrum. Methods A **299**, 166 (1990).
[38] S. J. Yennello, Ph.D. thesis, Indiana University, 1991.
[39] L. G. Moretto, Nucl. Phys. **A247**, 211 (1975).
[40] M. E. Fisher, Physics (N.Y.) **3**, 255 (1967).
[41] R. Trockel *et al.*, Prog. Part. Nucl. Phys. **15**, 225 (1985); Phys. Rev. C **39**, 729 (1989).
[42] J. L. Wile *et al.*, Phys. Rev. C **45**, 2300 (1992).
[43] Y. Yariv and Z. Frankel, Phys. Rev. C **20**, 2227 (1979); **26**, 2138 (1982).
[44] J. Cugnon, T. Mizutani, and J. Vandermuellen, Nucl. Phys. **A352**, 505 (1981).
[45] J. Cugnon, D. Kinet, and J. Vandermuellen, Nucl. Phys. **A379**, 553 (1982).
[46] J. Bondorf, R. Donangelo, I. N. Mishustin, and H. Schulz, Nucl. Phys. **A444**, 460 (1985).
[47] K. Kwiatkowski, W. A. Friedman, L. W. Woo, V. E. Viola, C. Volant, E. C. Pollacco, and S. J. Yennello, Indiana University Report No. INC-40007-89, 1992 (submitted to Phys. Rev. C).
[48] N. T. Porile, Phys. Rev. **120**, 572 (1960).
[49] F. Saint-Laurent, M. Conjeaud, R. Dayras, S. Harar, H. Oeschler, and C. Volant, Phys. Lett. **110B**, 372 (1982).
[50] V. E. Viola, Nucl. Phys. **A471**, 53c (1987); L. W. Woo, K. Kwiatkowski, and V. E. Viola, Phys. Lett. **132B**, 283 (1983).
[51] X. Campi *et al.*, in Proceedings of the International Conference on Theoretical Approaches to Heavy Ion Reaction Mechanisms, Paris, 1984 (unpublished).
[52] J. Lopez and J. Randrup, Nucl. Phys. **A491**, 477 (1989).
[53] D. Cebra *et al.*, Phys. Rev. Lett. **64**, 2246 (1990).
[54] J. Bondorf, C. H. Dasso, R. Donangelo, and G. Pollarolo, Phys. Lett. B **240**, 28 (1990).
[55] R. Charity *et al.*, Nucl. Phys. **A483**, 371 (1988).
[56] W. W. Wilcke, J. R. Birkelund, H. J. Wollersheim, A. D. Hoover, J. R. Huizenga, W. U. Schröder, and L. E. Tubbs, At. Data Nucl. Data Tables **25**, 389 (1980).
[57] J. Cugnon and C. Volant, Z. Phys. A **334**, 435 (1989).
[58] J. Cugnon, Phys. Rev. C **22**, 1885 (1980).
[59] M. Cubero, M. Schönhoffen, B. L. Friman, and W. Nörenberg, Nucl. Phys. **A519**, 345c (1990).